Quantum dynamics of topological strings in a frustrated Ising antiferromagnet (Supplementary materials)

Zheng Zhou (周正), Changle Liu (刘长乐), Zheng Yan (严正), Yan Chen (陈焱), and Xue-Feng Zhang (张学锋)

CONTENTS

SUPPLEMENTARY FIGURE 1. COMPARISON WITH NEUTRON SPECTRUM

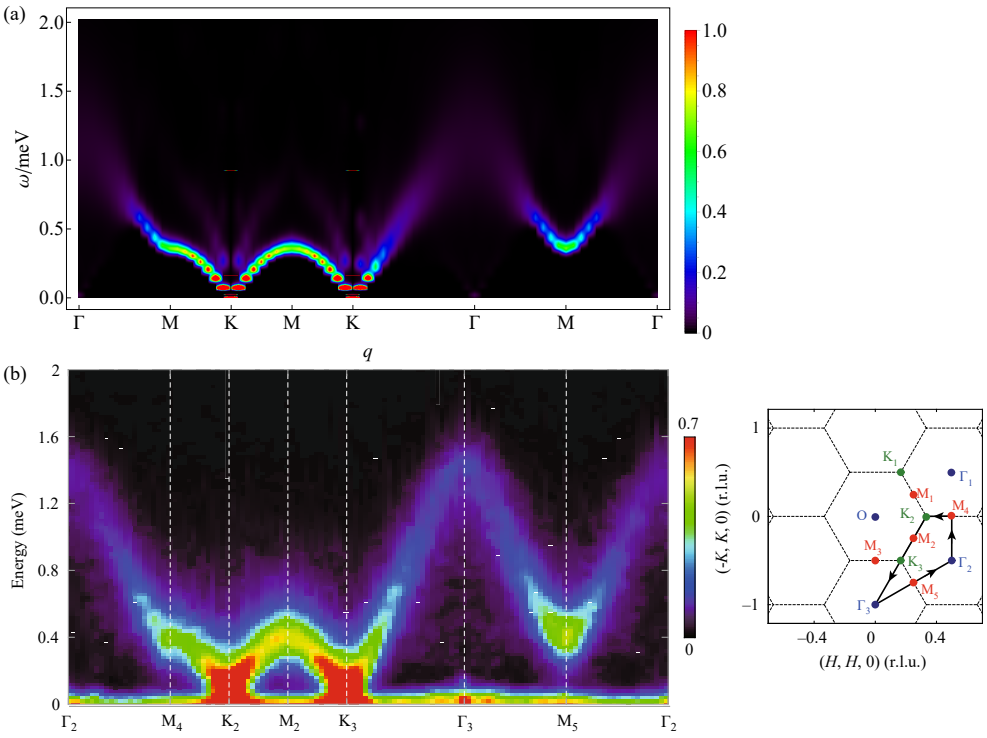

Supplementary Figure 1. (a) The QMC-SAC simulation of the S^{zz} spectrum, measured at $J = 0.99$meV, $J' = 0.05$meV and $\Delta = 0.54$meV, $L = 24$ and $\beta J = 96$; (b) the inelastic neutron scattering result in $TmMgGaO_4$, reproduced from Ref. [1].

In Supplementary Figure 1, we show that the QMC-SAC simulation on the antiferromagnetic Ising model with next-neareast-neighbour coupling and transverse field can reproduce the spectrum measured by inelastic neutron scattering [1] on $TmMgGaO_4$. As indicated by Ref. [2], the best fit parameters are found to be $J = 0.99$meV, $J' = 0.05$meV and $\Delta = 0.54$meV. In the Fig. 1 of main text we have plotted the numerical results of the spectrum at such parameters in logarithm scale coloring so that the two modes can both be seen clearly. To compare this QMC-SAC spectrum with the neutron scattering result, we plotted the spectrum in linear scale coloring and take meV as the energy unit. The spectrum from numerical simulation in Panel **a** and that from neutron scattering in Panel **b** agrees considerably well.

SUPPLEMENTARY FIGURE 2. SPECTRA IN LINEAR SCALE

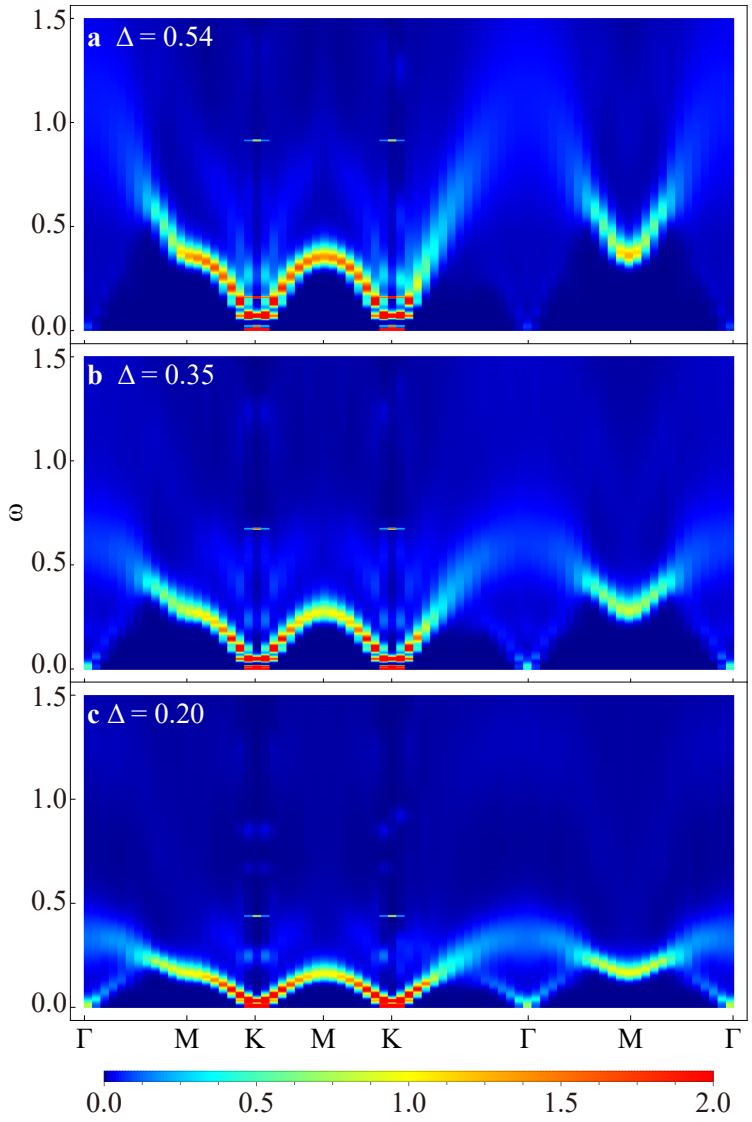

Supplementary Figure 2. The spectra at different transverse field Δ (Fig. 1 in main text) plotted in linear scale at $\Delta = 0.54$, $J' = 0.05$ (**a**), $\Delta = 0.35$, $J' = 0.035$ (**b**) and $\Delta = 0.20$, $J' = 0.020$ (**c**).

In Supplementary Figure 2, we replot the the spectra at different transverse field Δ in Fig. 1 in the main text in linear scale.

SUPPLEMENTARY FIGURE 3. RELIABILITY CHECK OF STOCHASTIC ANALYTICAL CONTINUATION

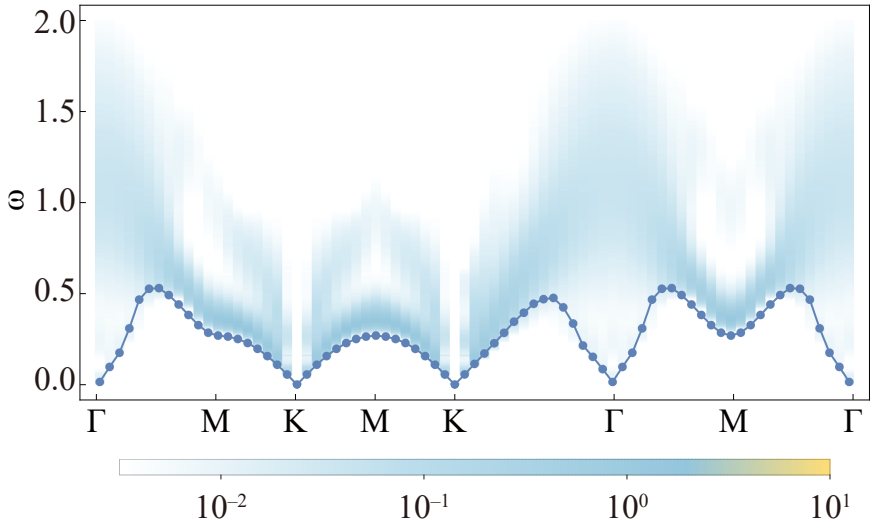

Supplementary Figure 3. The spectrum calculated by the SAC, plotted together with lowest excitation frequency extracted directly from the imaginary time correlations. The data are measured at $\lambda = 1, \Delta = 0.54, J' = 0.05$, same as Fig. 1a in the manuscript.

In Supplementary Figure 3, as an evidence of the validity of SAC, we also compare the spectral function obtained from SAC with the lowest excitation frequency extracted directly from the imaginary time correlations. As $G(\tau) \sim \int_0^\infty \mathrm{d}\tau\, S(\omega) \exp(-\omega\tau)$, at large τ, only the lowest energy ω_m retains. Thus, we obtain ω_m by performing the fitting $G(\tau) \sim \exp(-\omega_m \tau)$ for $0.2\beta < \tau < 0.4\beta$. The fitted ω_m agrees well with the low energy boundary of the SAC spectrum.

SUPPLEMENTARY FIGURE 4. VISUALISATION OF STRINGS

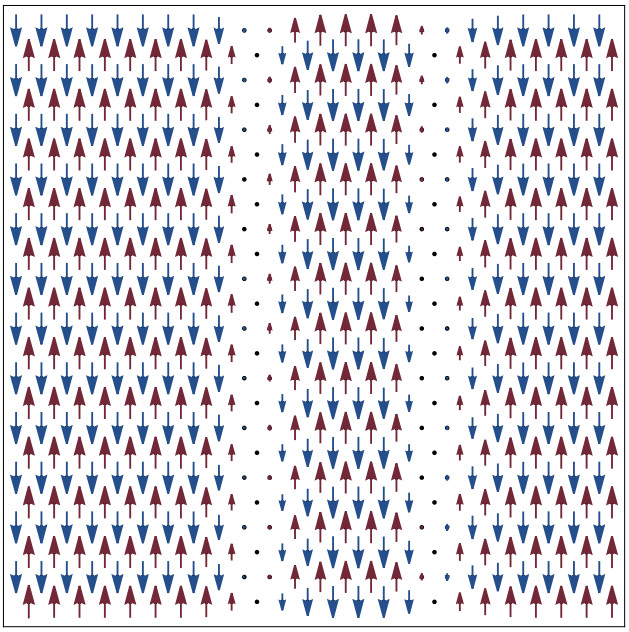

Supplementary Figure 4. The snapshot of the real space spin correlation $G(\mathbf{r}) = \langle S^z(\mathbf{r})S^z(0)\rangle$ measured at $\lambda = 0.893, N_s = 2$ in $L = 24$ system. The strings fluctuate in the regions with weak spin correlation.

It is possible to observe string-like configurations from Monte Carlo simulations. As an evidence, in Supplementary Figure 4 we measured a snapshot of the real-space spin correlation function $G(\mathbf{r}) = \langle S^z(\mathbf{r})S^z(0)\rangle$ at $\lambda = 0.893, N_s = 2$ in $L = 24$ system with rectangular periodic boundary within a short number of Monte Carlo steps, from which one can easily recognise the different stripe domains and the average string configuration as their domain walls. The average correlation near the strings are weak, revealing the strong fluctuation between two domains in this region.

SUPPLEMENTARY NOTE 1. DIMER AND STRING MAPPING

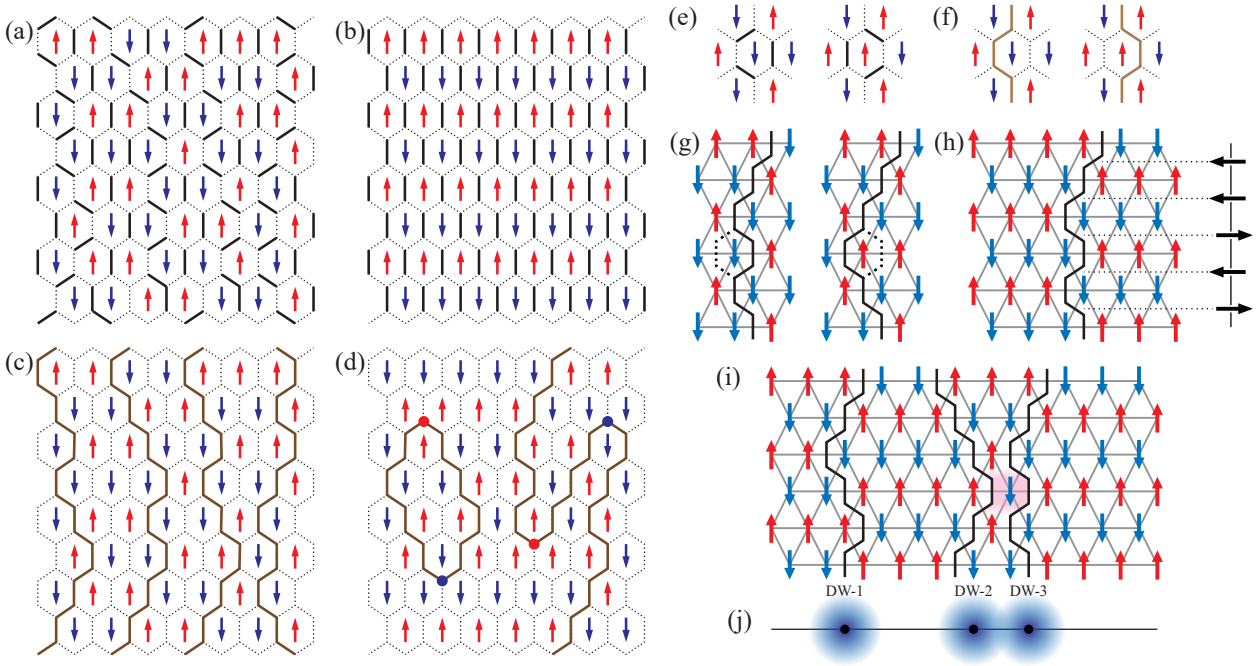

Figure for Supplementary Note 1. (a) Mapping of a spin configuration to a dimer covering on the dual hexagonal lattice; (b) the reference state of string mapping; (c) mapping a dimer covering to a string configuration and flippable spins are highlighted; (d) vortex and antivortex connected by two strings; (e) The dimer representation and (f) the string representation of flipping a flippable spin; (g) The deformation of the string by flipping spin; (h) The spin configuration with one string which can be mapped to spin-1/2 chain; (g) The spin configuration with three strings. At low temperature and small transverse field, the strings can not be crossed with each other (spin inside the red region can not flip due to triangle-rule), so that there exists effective interactions between strings; (h) The configuration in upper panel can be taken as three fermions with long-range effective interactions in one dimension.

In this section we give a detailed description of the mapping between the spin configuration and the dimer configuration, and between the dimer configuration and the string configuration. The spin configuration is defined on triangular lattice. The dual lattice of this triangular lattice is a honeycomb lattice (Panel **a**). Each bond of the dual lattice sits on the perpendicular bisector of a bond of the original lattice. Each site of the original lattice is mapped onto a hexagonal plaquette of the dual lattice, and the six nearest-neighbour bonds connecting one site on the original lattice become the six edges of a hexagon on the dual lattice. Reciprocally, the triangles on the original lattice become the sites on the dual lattice, and the three bonds along the triangle are mapped onto the bonds connecting one site on the dual lattice.

On this dual triangular lattice we can obtain the dimer representation of the spin configuration, where the

degree of freedom resides on the bonds, i.e., each bond is either occupied or unoccupied with a dimer. Each original bond connecting parallel original spins is mapped into a dual occupied dimer, whereas each original bond connecting antiparallel spins is mapped into a dual unoccupied dimer (Panel **a**). The antiferromagnetic Ising coupling imposes on the original lattice the triangle rule, which dictates that one triangle either have two spin-downs and one spin-up, or two spin-ups and one spin-down. This constraint is mapped to an one-dimer-per-site constraint on the dual lattice. As each triangle satisfying the triangle rule on the original lattice is composed of two antiparallel bonds and one parallel bonds, each site on the dual lattice is connected to two unoccupied bons and one occupied bond.

In this dimer representation we can further interpret the dynamics brought by the transverse field. To satisfy the constraint, the transverse field can only act on the spins such that three of its nearest neighbours point up and the other three point down, at the same time spin-ups and spin-downs appear alternatively. Such spins corresponds to the hexagonal plaquettes with three dimers and the occupied and unoccupied bonds appear alternatively (Panel **e**). By acting the transverse field, the spin is flipped, which exchanges its neighbouring bonds connecting parallel spins with bonds connecting antiparallel spins. On the dual lattice, this process corresponds to turning the occupied bonds into unoccupied bonds and vice versa on a hexagonal plaquette, which is exactly the dynamics of the off-diagonal term in the quantum dimer model. N.b., to keep the constraint, the transverse field has to be a perturbation with respect to the Ising term. In this way, the transverse field antiferromagnetic Ising model on triangular lattice is mapped exactly to a quantum dimer model with only the off-diagonal term, i.e., at $t/V = 0$.

The dimer configuration can be further mapped onto a string configuration, where each site is connected to not one, but an even number of occupied links, and the links form closed loops. To perform the mapping, a reference configuration must be taken. Here we take the staggered dimer configuration where all the bonds in one direction are occupied (Panel **b**). This state corresponds to the stripe state in the original spin configuration. We then collapse the dimer configuration with the reference configuration. Each bond which is covered exactly once by the dimer configuration and the reference configuration is mapped into an occupied bond in the string configuration, while the bonds covered twice or uncovered by the two configurations are mapped into unoccupied bonds (Panel **c**). In this way, the dimers in dimer configuration are joint into directed, non-crossing closed strings which crosses the boundary in periodic boundary condition.

Another way to understand such string configuration is to view it as a topological defect or domain wall on the original spin configuration, with respect to the stripe phase. Each original bond in x-direction connecting antiparallel spins is crossed by a string defined hereinbefore, i.e., each string is a domain wall which separates distinct stripe domains.

Therefore we can analysis the dynamics in the string language. the flippable spins situate in the corners of the strings (Panel **g**). By flipping the spin with transverse field, the related strings are deformed in the form of creation or annihilation of kinks. E.g., in Panel **f**, when flipping the spin, the string on its left deforms to its right.

The deformation of a single string can be analysed by mapping it to an effective spin model. Each string can be mapped into a spin-$1/2$ chain in the way that a left-going or right-going string segment is mapped into a spin-up or a spin-down respectively (Panel **h**). In this way the corners of the string are mapped into the kinks on the effective spin chain which separate antiparallel effective spins. By flipping the original spin inside the string corner, the left-going and right-going segment on the string is exchanged, i.e., the neighbouring spin-up and spin-down is exchanged. This corresponds to an effective XY interaction on the effective spin chain. In this way we can write down the effective Hamiltonian for a single string

$$H_{\text{str}} = \frac{\Delta}{4} \sum_{\langle ij \rangle} (\sigma_i'^{+} \sigma_j'^{-} + \sigma_i'^{-} \sigma_j'^{+}) \tag{1}$$

Here $\sigma'_{i,j}$ denotes the effective spins of the string and $\sigma'^{\pm}$ are the ladder operators. The $\langle ij \rangle$ denotes that the sum is taken over all the nearest neighbours. This model is well studied and is exactly solvable under Jordan-Wigner transformation. Its excitations are free fermions in the form of effective "spinons" on the effective spin chain and "kinks" in the spin representation on the original lattice.

The discussion above only considers single string case. When multiple strings appear in one configuration at the same time, they have to conform with the non-crossing condition. This condition is equivalent with the triangle rule in spin representation and the one-dimer-per-site constraint in dimer representation. Such condition restricts the Hilbert space of the strings. Same as the spin-$1/2$ chain, the size of a single string's Hilbert space is 2^{L_y}. However, when two strings get close (e.g., the string 2 and 3 in Panel **i**), certain configurations with crossing strings are forbidden. So that the Hilbert space shrinks and an effective long-range interaction emerges (Panel **i**). Such interaction is found repulsive and should be algebraic to the distance between strings [3]. On the contrary, violation of this rule results in the triangles with three parallel spins. Such triangle hosts a spinon excitation, which is also known as "vortex" as the winding number of effective $U(1)$ spin is non-zero [2]. The vortices are connected by either a string loop or a non-directed string (Panel **d**).

SUPPLEMENTARY NOTE 2. INCOMMENSURATE ORDER

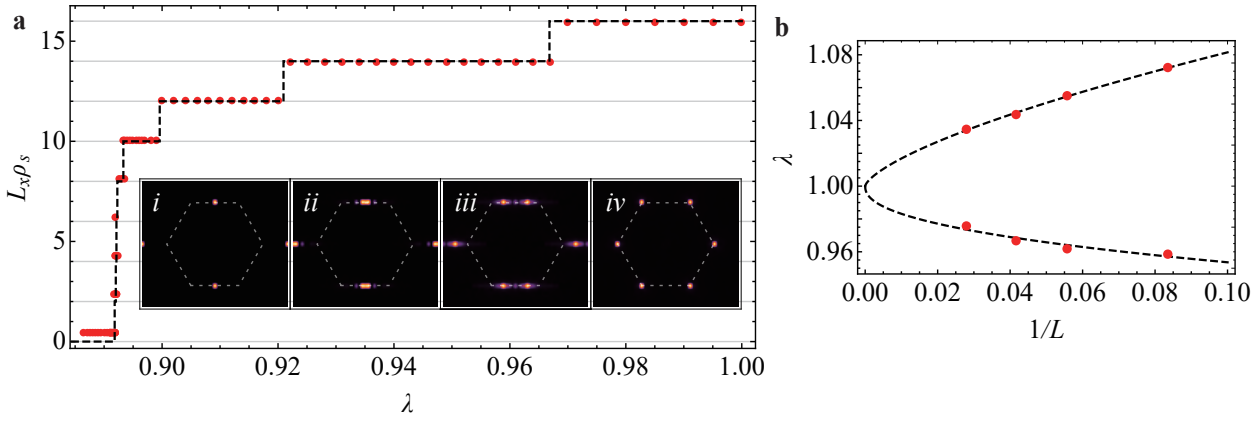

Figure for Supplementary Note 2. (a) the string density–anisotropy relation, measured at $\beta = L = 24$ and $J' = 0$; Inset : The magnetic structure factor with different string density, at (i) $\lambda = 0.89$, $\rho_s = 0$ (stripe phase); (ii) $\lambda = 0.892$, $\rho_s = 1/12$; (iii) $\lambda = 0.895$, $\rho_s = 1/3$; and (iv) $\lambda = 1.00$, $\rho_s = 2/3$; (b) The finite size scaling result for the upper and lower boundary of the clock order plateau $\rho_s = 2/3$.

By decreasing λ from 1, the string density ρ_s, defined as

$$\rho_s = \frac{1}{N}\sum_{\langle ij\rangle_x}\frac{1-4S_i^zS_j^z}{2} \tag{2}$$

which effectively counts the number of horizontal bonds connecting opposite spins, drops from $2/3$ and finally reach zero (Panel **a**) as the system enters the stripe phase through a continuous phase transition. Accordingly, the peak of magnetic structure factor

$$S(\mathbf{q}) = \frac{1}{N}\sum_{ij}\langle S_i^zS_j^z\rangle \exp\left(i\mathbf{q}\cdot(\mathbf{r}_i-\mathbf{r}_j)\right) \tag{3}$$

moves from K to M linearly with the string density (Panel **a** inset), in accordance with the theoretical expectation of wave vector $\mathbf{q} = (\pm(2-\rho_s),0)\pi$ and $(\pm\rho_s, \pm 2/\sqrt{3})\pi$.

It should also be noted that the structure of plateaux with discrete jumps is a result of the topological nature of the strings together with the finite size effect. Each of the plateau corresponding to an even integer number of domain walls $N_s = \rho_s L_x$. The platforms and jumps become increasingly continuous for larger system scale. A finite-size scaling (Panel **b**) of the left and right jumping point of the $\rho_s = 2/3$ platform corresponding to the clock phase demonstrate that in the thermodynamic limit the domain wall density should be a continuous function of J_x.

SUPPLEMENTARY NOTE 3. RESEMBLANCE TO THE LUTTINGER LIQUID

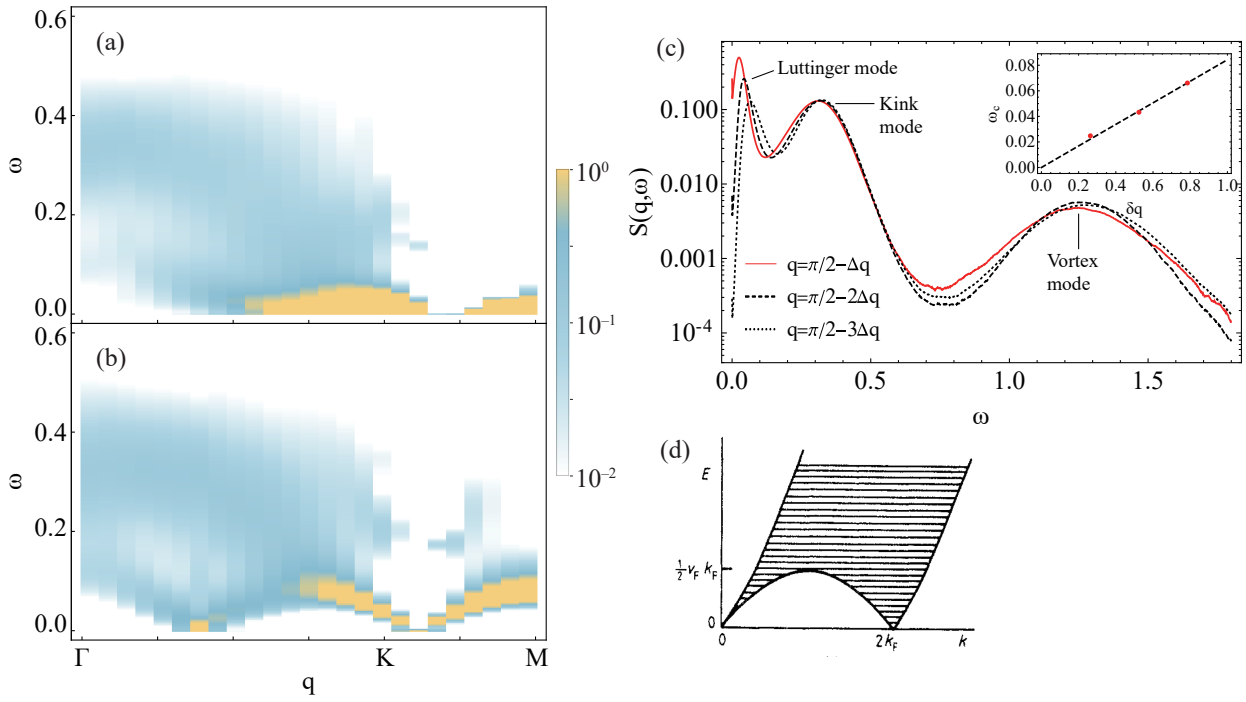

Figure for Supplementary Note 3. The low frequency region of S^{zz} spectra along x-direction measured at (a) $\rho_s = 1/3$, $J_x = 0.895$ and (b) $\rho_s = 1/2$, $J_x = 0.91$, the dashed lines show the correspondence to Luttinger liquid; (c) the spectral function at momenta in vicinity of $q = \pi/2$; inset: the center of Luttinger mode as a function of momentum deviation at $\rho_s = 1/2$, $J_x = 0.91$. $L_x = L_y = 24$ and $\beta = 96$ is taken, $\Delta q = 2\pi/L_x$ is the minimal momentum interval; (d) The particle-hole spectrum of Luttinger liquid, reproduced from Ref. [4].

In this section, we demonstrate that the features in the S^{zz} spectrum at low string density ρ_s are reminiscent of the Luttinger liquid when we add an anisotropy As described previously, in the perpendicular direction, the strings can be viewed as 0D fermions moving on 1D line. There exists a long-range power-law repulsive interaction between adjacent fermions. As indicated in Ref. [5], this may result in a Luttinger liquid phase at certain parameter region.

The spectrum of an one dimensional Luttinger liquid is characterized by two gapless points at $q = 0$ and $q = 2k_F$, measured from the Fermi surface, where k_F denotes the Fermi wave vector. The k_F is a function of the string density ρ_s (or particle density in the 1D)

$$k_F = \pi\rho_s \tag{4}$$

In the S^{zz} spectrum, the $q = 0$ point is mapped to $\mathbf{q} = ((2-\rho_s)\pi, 0)$, and the $q = 2k_F$ point is mapped to

$\mathbf{q} = ((2 - 3\rho_s)\pi, 0)$. The dispersion in vicinity of these gapless points are linear. These two gapless points and the linear dispersion in vicinity are indeed observed in numerical results (Panel **a**, **b**).

We then scrutinize the spectra at momenta in vicinity of the $q = 2k_F$ point (Panel **c**). Three distinct peak is observed. The lowest mode owns a frequency proportional to the momentum deviation, thus corresponds to the excitations of Luttinger liquid. The medium mode situates near the frequency of transverse field Γ, thus corresponds to the kink excitation (or the effective spinon excitation in the effective XY model). These two peaks together compose the excitations related to quantum strings. The highest mode corresponds to the triangle-rule breaking vortex excitation at the energy scale of J.

SUPPLEMENTARY NOTE 4. DEFINITION OF KINK AND VORTEX OPERATOR

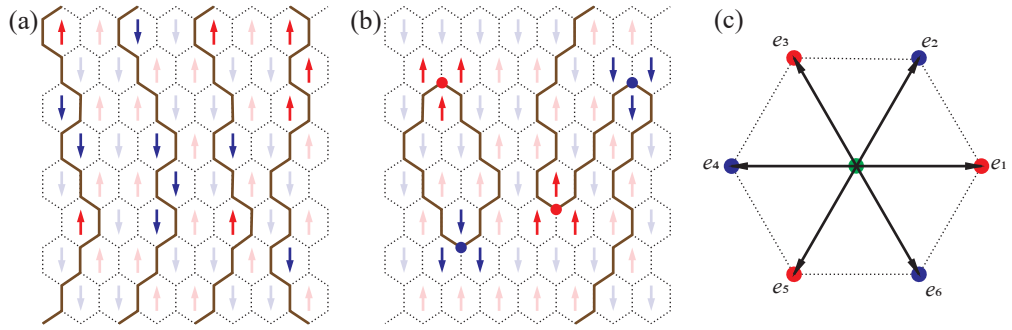

Figure for Supplementary Note 4. Demonstration of the kink and vortex operator. The red up arrows and blue down arrows show where (a) kink operator and (b) vortex operator is non-zero, whereas the whitened arrows show where the operators vanish.

To isolate the contributions from string and vortex mode, we define the kink and vortex operator. The spectra calculated from their correlation can effectively distinguish the strength of S^{zz} spectrum which comes from string and vortex mode. These two operators single out the spins concerned with corresponding excitation.

For the string mode we define a kink operator. As mentioned before, the dynamics of the strings can be mapped into an effective spin-$1/2$ chain with XY nearest neighbour coupling. The excitation of such chain is fermions known as kinks residing on each bond connecting opposite effective spins. This corresponds to the corners of strings in the 2D string representation. In the spin representation, the spin envelopped by the corner has three spin-ups and three spin-downs as its neighbours which appear alternatively. This can be used as a criteria to single out the kinks. The kink operator is defined on each site of the spin configuration. It is non-zero only on the sites which is envelopped by a corner of the string, or to written explicitly,

$$\mathscr{K}(\mathbf{r}) = \begin{cases} S(\mathbf{r}), & \text{if } S(\mathbf{r}+\mathbf{e}_1) = -S(\mathbf{r}+\mathbf{e}_2) = S(\mathbf{r}+\mathbf{e}_3) \\ & \quad = -S(\mathbf{r}+\mathbf{e}_4) = S(\mathbf{r}+\mathbf{e}_5) = -S(\mathbf{r}+\mathbf{e}_6) \\ 0, & \text{elsewhere.} \end{cases} \tag{5}$$

where $\mathbf{e}_i$ is the displacement from a site to its six neighbours (Panel **c**). N.b., this definition is equivalent to singling out the "flippable" spins.

On the other hand, for the vortex mode we define a vortex operator. In the original spin representation, the vortices take the form of a triangle with three parallel spins. So we just have to single out the spins which

belong to triangles with parallel spins, or to written explicitly

$$\mathscr{V}(\mathbf{r}) = \begin{cases} S(\mathbf{r}), & \text{if } S(\mathbf{r}) = S(\mathbf{r}+\mathbf{e}_1) = S(\mathbf{r}+\mathbf{e}_2) \text{ or } S(\mathbf{r}) = S(\mathbf{r}+\mathbf{e}_2) = S(\mathbf{r}+\mathbf{e}_3) \\ & \text{or } S(\mathbf{r}) = S(\mathbf{r}+\mathbf{e}_3) = S(\mathbf{r}+\mathbf{e}_4) \text{ or } S(\mathbf{r}) = S(\mathbf{r}+\mathbf{e}_4) = S(\mathbf{r}+\mathbf{e}_5) \\ & \text{or } S(\mathbf{r}) = S(\mathbf{r}+\mathbf{e}_5) = S(\mathbf{r}+\mathbf{e}_6) \text{ or } S(\mathbf{r}) = S(\mathbf{r}+\mathbf{e}_6) = S(\mathbf{r}+\mathbf{e}_1) \\ 0, & \text{elsewhere.} \end{cases} \tag{6}$$

SUPPLEMENTARY NOTE 5. COMPARISON WITH SPIN WAVE METHODS

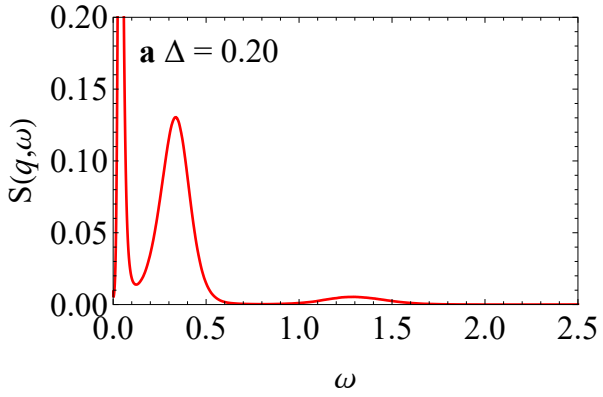

Figure for Supplementary Note 5. The spectral function $S(\mathbf{q},\omega)$ at momentum $q_x = \Delta q = 2\pi/L, q_y = 0$ measured at $\Gamma = 0.2$, plotted in linear scale

In this section, we compare our string description with the spin wave descriptions that have been formerly used to study the spectrum of rare-earth compounds.

First, the spin wave theories are semi-quantitative theories. Particularly, in frustrated magnets, quantum fluctuation is largely neglected in spin waves. As a matter of fact, the predicted parameters, especially the transverse field Δ, for TMGO by spin wave theory deviates a lot from those extracted by more methods such as QMC. Therefore, tuning parameters away from their physical value is needed to produce spectra that agree with numerics or experiments.

By contrast, our string picture can produce quite simple and effective quantitative predictions in a wide range of system parameters. The most representative example is the envelop of continuum excitations. Along ΓM direction, we predict that the excitations correspond to kinks inside each string, and the spectra are enveloped by the sine curves $\omega_1 = \Delta \cos \sqrt{3} k_y/2$ and $2\Delta \cos \sqrt{3} k_y/4$, which agrees considerably well with numerical results (Fig. 3b in main text). Along ΓKM direction, we predict the excitations correspond to Luttinger liquids above the energy scale of the gap. The nearly gapless point should lie at $k_x = 2\pi - \pi\rho_s$ and $k_x = 2\pi - \pi\rho_s$, and the dispersions in vicinity should be linear, which also agree with our numerical results. As far as we know, our string picture is the simplest theory that explains these features altogether.

Meanwhile, some features of our spectrum are hard to be reproduced by spin wave theories. For example, at low transverse field $\Delta = 0.2$, in vicinity of Γ point, we find three instinct peaks in the spectrum, centered at $\omega = 0.038, 0.337$ and 1.302 respectively, composing $37\%, 58\%$ and 5% of the spectrum weight. These three peaks are explained in our string picture as the excitation due to interstring interaction, kink-antikink

pair on single string and the spinons, respectively. On the other hand, spin wave theory only predicts the existence of two peaks — two of the three modes in the linear spin wave are degenerate at Γ point required by degeneracy, as shown in Fig. 9 of Ref. [6]. The two modes predicted by LSW corresponds to the highest frequency and lowest frequency peak in the spectrum we find. The peak that makes up the largest portion of weight is missed in the linear spin wave theory. This peak is unlikely to come from the non-linear corrections as well, since its weight is larger than the LSW contribution.

Our string picture becomes more rigorous and provide richer physics when we consider anisotropic NN interactions. In this case, the spatial anisotropy can stabilize the incommensurate phase out of the commensurate clock phase. The incommensurate order wave vector exhibits a linear relation with the string density. In the string picture, by minimizing the string energy, we are able to predict a string density-anisotropy relation that agrees with the numerical results (See Supplementary Note 1, 2). We are also able to clearly visualise the strings in the spin configuration snapshot (See Supplementary Figure 4). Furthermore, at low string density with weak inter-string interactions, the spectra exhibit clearer continuous features with agree perfectly with the effective model.

SUPPLEMENTARY METHOD 1. STOCHASTIC SERIES EXPANSION (SSE)

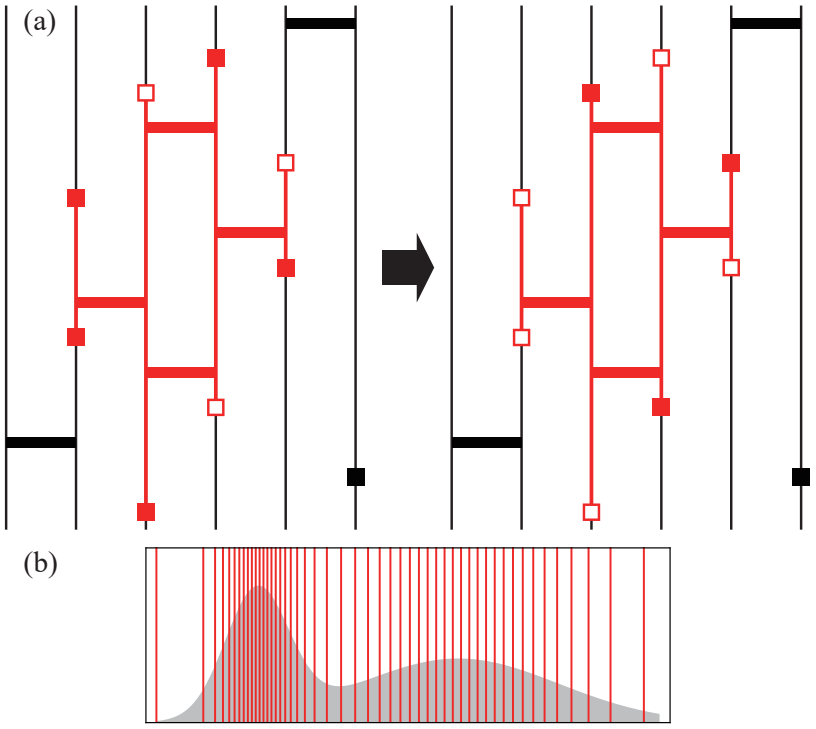

Figure for Supplementary Methods. (a) An illustration of the SSE cluster update process where the cluster marked in red is identified and flipped as a whole. A vertical line shows a spin expanded. The solid and empty squares show the diagonal and off-diagonal site operators. The solid bars show the diagonal bond operators. (b) An illustration of the parametrization of a continuous spectral function into discrete δ-functions.

For the numerical works in this paper, we use a quantum Monte Carlo (QMC) method with stochastic series expansion (SSE) algorithm[7–9] to calculate the ground state properties and imaginary time Green function. This method will be briefly introduced below.

In quantum statistics, the measurement of observables is closely related to the calculation of partition function Z

$$\langle \mathscr{O} \rangle = \mathrm{tr}\ \left(\mathscr{O} \exp(-\beta H)\right)/Z, \quad Z = \mathrm{tr} \exp(-\beta H) \tag{7}$$

where $\beta = 1/T$ is the inverse temperature, H is the Hamiltonian of the system and $\mathscr{O}$ is an arbitrary observable. Typically, in order to evaluate the ground state property, one takes a sufficiently large β such that $\beta \sim L^z$, where L is the system scale and z is the dynamical exponent. In SSE, such evaluation of Z is done by a Taylor expansion of the exponential and the trace is taken by summing over a complete set of

suitably-chosen basis.

$$Z = \sum_{\alpha} \sum_{n=0}^{\infty} \frac{\beta^n}{n!} \langle \alpha | (-H)^n | \alpha \rangle \tag{8}$$

We then write the Hamiltonian as the sum of a set of operators whose matrix elements are easy to calculate.

$$H = -\sum_{i} H_i \tag{9}$$

In practice we truncate the Taylor expansion at a sufficiently large cutoff M and it is convenient to fix the sequence length by introducing in identity operator $H_0 = 1$ to fill in all the empty positions despite it is not part of the Hamiltonian.

$$(-H)^n = \sum_{\{i_p\}} \prod_{p=1}^{n} H_{i_p} = \sum_{\{i_p\}} \frac{(M-n)!n!}{M!} \prod_{p=1}^{n} H_{i_p} \tag{10}$$

and

$$Z = \sum_{\alpha} \sum_{\{i_p\}} \beta^n \frac{(M-n)!}{M!} \langle \alpha | \prod_{p=1}^{n} H_{i_p} | \alpha \rangle \tag{11}$$

To the carry out the summation, a Monte Carlo procedure can be used to sample the operator sequence $\{i_p\}$ and the trial state α with according to their relative weight

$$W(\alpha, \{i_p\}) = \beta^n \frac{(M-n)!}{M!} \langle \alpha | \prod_{p=1}^{n} H_{i_p} | \alpha \rangle \tag{12}$$

For sampling we adopt a Metropolis algorithm where the configuration of one step is generated based on updating the configuration of the former step and the update is accepted at a probability

$$P(\alpha, \{i_p\} \to \alpha', \{i'_p\}) = \min\left(1, \frac{W(\alpha', \{i'_p\})}{W(\alpha, \{i_p\})}\right) \tag{13}$$

Diagonal update, where diagonal operators are inserted into and removed from the operator sequence, and cluster update, where diagonal and off-diagonal operates convert into each other, are adopted in update strategy.

In transverse field Ising model $H = J \sum_b S^z_{i_b} S^z_{j_b} - h \sum_i \sigma^x_i$, we write the Hamiltonian as the sum of following operators

$$\begin{aligned} H_0 &= 1 \\ H_i &= h(S^+_i + S^-_i)/2 \\ H_{i+n} &= h/2 \\ H_{b+2n} &= J(1/4 - S^z_{i_b} S^z_{j_b}) \end{aligned} \tag{14}$$

where a constant is added into the Hamiltonian for convenience. For the non-local update, a branching cluster update strategy is constructed [8], where a cluster is formed in $(D+1)$-dimensional by grouping spins and operators together. Each cluster terminates on site operators and includes bond operators (Panel **a**). All the spins in each cluster is flipped together at a probability $1/2$ after all clusters are identified.

SUPPLEMENTARY METHOD 2. STOCHASTIC ANALYTICAL CONTINUATION (SAC)

For the spectra in this paper we adopted a stochastic analytical continuation (SAC) [10–12] method to obtain the spectral function $S(\omega)$ from the imaginary time correlation $G(\tau)$ measured from QMC, which is generally believed a numerically unstable problem. This method will be briefly introduced below.

The spectral function $S(\omega)$ is connected to the imaginary time Green's function $G(\tau)$ through an integral equation

$$G(\tau) = \int_{-\infty}^{\infty} \mathrm{d}\omega S(\omega) K(\tau, \omega) \tag{15}$$

where $K(\tau, \omega)$ is the kernel function depending on the temperature and the statistics of the particles. We restrict ourselves to the case of spin systems and with only positive frequencies in the spectral, where $K(\tau, \omega) = (e^{-\tau\omega} + e^{-(\beta-\tau)\omega})/\pi$. To ensure the normalization of spectral function, we further modify the transformation and come to the following equation :

$$G(\tau) = \int_{0}^{\infty} \frac{\mathrm{d}\omega}{\pi} \frac{e^{-\tau\omega} + e^{-(\beta-\tau)\omega}}{1 + e^{-\beta\omega}} B(\omega) \tag{16}$$

where $B(\omega) = S(\omega)(1 + e^{-\beta\omega})$ is the renormalized spectral function.

In practice, $G(\tau)$ for a set of imaginary time $\tau_i (i = 1, \cdots N_\tau)$ is measured in QMC simulation together with the statistical errors. The renormalized spectral function is parametrized into large number of equal-amplitude δ-functions whose positions are sampled (**b**)

$$B(\omega) = \sum_{i=0}^{N_\omega} a_i \delta(\omega - \omega_i) \tag{17}$$

Then the fitted Green's functions $\tilde{G}_i$ from Eq. 16 and the measured Greens functions $\bar{G}_i$ are compared by the fitting goodness

$$\chi^2 = \sum_{i,j=1}^{N_\tau} (\tilde{G}_i - \bar{G}_i)(C^{-1})_{ij}(\tilde{G}_j - \bar{G}_j) \tag{18}$$

where the covariance matrix is defined as

$$C_{ij} = \frac{1}{N_B(N_B - 1)} \sum_{b=1}^{N_B} (G_i^b - \bar{G}_i)(G_j^b - \bar{G}_j), \tag{19}$$

with N_B the number of bins, the measured Green's functions of each G_i^b.

A Metropolis process is utilized to update the series in sampling. The weight for a given spectrum is taken to follow a Boltzmann distribution

$$W(\{a_i, \omega_i\}) \sim \exp\left(-\frac{\chi^2}{2\Theta}\right) \tag{20}$$

with Θ a virtue temperature to balance the goodness of fitting χ^2 and the smoothness of the spectral function. All the spectral functions of sampled series $\{a_i, \omega_i\}$ is then averaged to obtain the spectrum as the final result.

[1] Y. Shen, Y.-D. Li, H. Wo, Y. Li, S. Shen, B. Pan, Q. Wang, H. Walker, P. Steffens, M. Boehm, *et al.*, Evidence for a spinon fermi surface in a triangular-lattice quantum-spin-liquid candidate, Nature **540**, 559 (2016).

[2] H. Li, Y. Da Liao, B.-B. Chen, X.-T. Zeng, X.-L. Sheng, Y. Qi, Z. Y. Meng, and W. Li, Kosterlitz-Thouless melting of magnetic order in the triangular quantum Ising material $TmMgGaO_4$, Nat. Commun. **11**, 1 (2020).

[3] X.-F. Zhang, S. Hu, A. Pelster, and S. Eggert, Quantum domain walls induce incommensurate supersolid phase on the anisotropic triangular lattice, Phys. Rev. Lett. **117**, 193201 (2016).

[4] F. D. M. Haldane, 'luttinger liquid theory' of one-dimensional quantum fluids. i. properties of the luttinger model and their extension to the general 1d interacting spinless fermi gas, J. Phys. C **14**, 2585 (1981).

[5] Z.-H. Li, Ground states of long-range interacting fermions in one spatial dimension, J. Phys. Cond. Matt. **31**, 255601 (2019).

[6] G. Chen, Intrinsic transverse field in frustrated quantum ising magnets: Physical origin and quantum effects, Phys. Rev. Research **1**, 033141 (2019).

[7] A. W. Sandvik, Finite-size scaling of the ground-state parameters of the two-dimensional heisenberg model, Phys. Rev. B **56**, 11678 (1997).

[8] A. W. Sandvik, Stochastic series expansion method for quantum ising models with arbitrary interactions, Phys. Rev. E **68**, 056701 (2003).

[9] A. Avella and F. Mancini, *Strongly correlated systems: numerical methods*, Vol. 176 (Springer Science & Business Media, 2013).

[10] A. W. Sandvik, Stochastic method for analytic continuation of quantum monte carlo data, Phys. Rev. B **57**, 10287 (1998).

[11] H. Shao, Y. Q. Qin, S. Capponi, S. Chesi, Z. Y. Meng, and A. W. Sandvik, Nearly deconfined spinon excitations in the square-lattice spin-1/2 heisenberg antiferromagnet, Phys. Rev. X **7**, 041072 (2017).

[12] A. W. Sandvik, Constrained sampling method for analytic continuation, Phys. Rev. E **94**, 063308 (2016).